Research Square

Preprints are preliminary reports that have not undergone peer review.
They should not be considered conclusive, used to inform clinical practice,
or referenced by the media as validated information.

A wetter yet drier world: the role of intensified precipitation unevenness

Zhiyan Zuo

zuozhy@fudan.edu.cn

Fudan University https://orcid.org/0000-0001-5708-723X

Sijie Chen

Department of Atmospheric and Oceanic Sciences/Institute of Atmospheric Sciences, Fudan University

Meiyu Chang

Department of Atmospheric and Oceanic Sciences/Institute of Atmospheric Sciences, Fudan University

Deliang Chen

Tsinghua University https://orcid.org/0000-0003-0288-5618

Kaiwen Zhang

Fudan University

Renhe Zhang

Fudan University https://orcid.org/0000-0001-7750-8679

Article

Keywords:

Posted Date: November 9th, 2026

DOI: https://doi.org/10.21203/rs.3.rs-11413248/v1

License: This work is licensed under a Creative Commons Attribution 4.0 International License.
Read Full License

Additional Declarations: There is **NO** Competing Interest.

A wetter yet drier world: the role of intensified precipitation unevenness

Sijie Chen[1,3], Meiyu Chang[1,3], Zhiyan Zuo[1*], Deliang Chen[2], Kaiwen Zhang[1], Renhe Zhang[1]

[1] *Key Laboratory of Polar Atmosphere-ocean-ice System for Weather and Climate of Ministry of Education/Shanghai Key Laboratory of Ocean-Land-Atmosphere Boundary Dynamics and Climate Change, Department of Atmospheric and Oceanic Sciences/Institute of Atmospheric Sciences, Fudan University, Shanghai 200438, China.*

[2] *Department of Earth System Science, Tsinghua University, Beijing 100084, China.*

[3] *These authors contributed equally: Sijie Chen, Meiyu Chang.*

*Corresponding author. Email: zuozhy@fudan.edu.cn

Abstract

Extensive increases in precipitation should have moistened the land surface, yet persistent soil drying has contradicted this expectation over recent decades. Here, we reveal that this hydrological paradox—more rainfall but drier soils—has emerged over two-fifths of global land. In these regions, rising precipitation is accompanied by a shift from low and moderate to heavy precipitation, channeling more water into rainfall that is poorly retained by the soil and less able to sustain soil moisture. This drying effect of increasing unevenness is roughly eleven times stronger than the wetting effect of increased total precipitation, causing soils to dry despite a wetter climate. Our results reveal the critical role of precipitation intensity distribution, rather than total amount, in shaping this hydrological contradiction.

A widespread drying trend in global surface soil has been observed in recent decades[1–3], leading to more frequent mega-heatwaves[4–6], worsening water crises[7,8], and mounting threats to ecological and food security[9,10]. As the direct input[11], precipitation has traditionally been regarded as the primary driver of soil moisture variability. However, despite a clear increase in total precipitation over most land regions under global warming—consistent with a theoretical rise of about 3% per kelvin[12]—soil moisture has continued to decline. This divergence between precipitation and soil moisture reveals a potential paradox: more rainfall yet drier soils, as reported in regions such as central North America [13,14] and Central Asia[15,16].

Beyond overall increases in precipitation, its temporal variability has risen markedly[17–23], and recent work reports that this unevenness has a negative impact on terrestrial water storage[24]. Meanwhile, although increased atmospheric evaporative demand has been proposed as a driver of soil moisture decline[25,26], the change in actual evapotranspiration remains highly uncertain at regional scales[27,28]. As such, a coherent picture of the extent to which soil aridification is impacted by increased precipitation amount and increased precipitation unevenness, together with the role of evapotranspiration, remains unclear.

Here, we investigate the quantitative effects of precipitation amount and unevenness on soil moisture trends across global land areas during 2000–2023 using observation-based datasets. Our results reveal that the widespread intensification of precipitation unevenness gives rise to paradoxical regions—spanning 42.4% of global land—by overriding the effect of total precipitation. In particular, increases in heavy

precipitation are identified as the primary drivers of enhanced precipitation unevenness. By reducing the effective precipitation stored in the soil and increasing runoff losses, this more concentrated precipitation distribution holds soil moisture and evapotranspiration at lower values, reshaping their distributions. Our work addresses the existing hydrological paradox by highlighting precipitation unevenness, providing novel insight for future drought prediction and mitigation, and supporting sustainable water management under climate change.

Paradox of a wetter climate and drier soils

To ensure a robust assessment, we constructed ensemble means by averaging the standardized time series from three precipitation datasets and five soil-moisture datasets, respectively (see Methods). Over the past two decades, 67.8% of the global land surface has experienced increasing precipitation (P+, Fig. 1a), yet soil moisture has declined across 74.6% of the surface (SM−, Fig. 1b), with agreement from at least two of the three precipitation datasets and three of the five soil-moisture datasets, respectively. This divergence gives rise to a paradoxical hydrological regime (P+SM−), covering 42.4% of ice-free land and largely overlapping with drylands (deep orange in Fig. 1d). The P+SM− regime occurs with high probability across these regions in all 15 precipitation–soil moisture dataset combinations (Supplementary Fig. 2), confirming that this widespread pattern is robust to dataset selection. Moreover, a similar inconsistency exists between spatial trends in water availability (precipitation minus evapotranspiration) and soil moisture (Supplementary Fig. 3), although earlier studies have emphasized the drying effect of increased evapotranspiration[25]. These results indicate that changes in total precipitation and evapotranspiration cannot fully explain the observed soil drying.

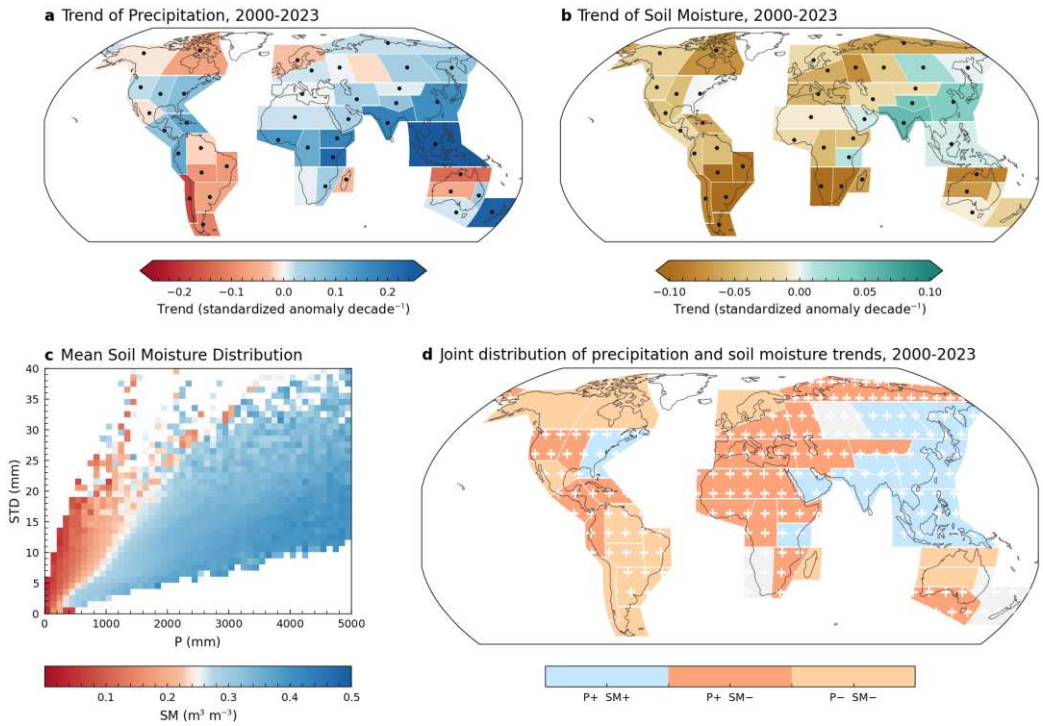


Fig. 1 | Trends in terrestrial precipitation, surface soil moisture, and their joint distribution over 2000–2023.

a, Trends in the standardized ensemble mean of annual total precipitation (P) from CPC, MSWEP and CHIRPS (see Methods). The boundaries correspond to the IPCC AR6 reference regions[31] (Supplementary Fig. 1), and the shading represents latitude-weighted averages calculated over the terrestrial areas within each region. Black dots indicate regions with cross-product agreement, where trends in at least two of the three precipitation products have the same sign as the ensemble trend. The same convention applies hereafter. **b**, Similar to panel **a**, but for annual mean surface soil moisture (SM) from GLEAM4, ERA5, ERA5-Land, ESA CCI and GLDAS-Noah. Black dots require agreement from at least three products. **c**, Relationship between annual total precipitation and precipitation unevenness (STD, defined as the standard deviation of within-year daily precipitation and derived from the same three precipitation products) across land. Color indicates mean soil moisture. **d**, Spatial distribution of three hydrological regimes, defined by the signs of the ensemble trends in precipitation and soil moisture (P+/P− and SM+/SM−). No region exhibits the P−SM+ regime. White crosses highlight regions with concurrent increases in precipitation unevenness. Only regions showing cross-product agreement in both P and SM are colored, while others are shown in gray.

Therefore, we propose that intensified unevenness in the temporal distribution of precipitation is probably the main driver of this mismatch. This unevenness is quantified by the standard deviation of precipitation, with higher values indicating greater temporal concentration—more rainfall occurring on fewer wet days rather than being evenly distributed. Between 2000 and 2023, all paradoxical regions have

experienced increases in precipitation unevenness (white crosses in Fig. 1d, Supplementary Fig. 4). The effect of precipitation unevenness on soil moisture is opposite to that of total precipitation: higher unevenness leads to drying, whereas increased precipitation promotes wetting (Fig. 1c). For instance, under similar total precipitation, soil moisture can fall from 0.3 to 0.1 m^3 m^{-3} as the precipitation unevenness rises from about 1 to 10 mm. In clay soils, such a drop would cross from near field capacity to below the permanent wilting point[29,30], shifting the soil from a plant-available state into severe water stress. This sensitivity is further quantified along the precipitation gradient, where a 1 mm increase in unevenness corresponds to a soil moisture decline of ~0.008, ~0.006, and ~0.003 m^3 m^{-3} at annual precipitation of 400, 800, and 1200 mm, respectively, with drier regions being disproportionately vulnerable to shifts in precipitation distribution.

Quantification of precipitation unevenness in soil drying

We quantify the relative contributions of precipitation amount and unevenness to soil moisture using a random forest model based on the ensemble means of all variables (see Methods, Supplementary Figs. 5–7). In most of paradoxical regions (P+SM−, second quadrant in Fig. 2a), unevenness emerges as the dominant contributor, where its negative contribution reaches nearly 11.4 times the positive contribution from precipitation amount (Fig. 2c). As a result, these regions continue to dry despite increasing precipitation. Other regimes exhibit either synchronous drying (P−SM−; 26.8%, primarily distributed in the Americas and Australia) or synchronous wetting (P+SM+; 24.4%, largely concentrated in monsoon-influenced regions), where

precipitation is the dominant control on soil moisture but the negative contribution from precipitation unevenness still exists. In the synchronous-drying regime, both declining precipitation amount and increasing unevenness impose negative impacts on soil moisture, with intensified precipitation variability amplifying the precipitation-driven deficit by roughly 31.0% (Fig. 2d). The drying effect of precipitation unevenness persists even where soils are net wetting. In the synchronous-wetting regime (Fig. 2b), rising precipitation amount drives a strong positive soil moisture trend, yet intensifying unevenness offsets roughly 44% of this gain. The observed wetting is therefore markedly weaker than the precipitation increase alone would cause.

These results highlight that shifts in precipitation variability, rather than changes in total precipitation or evapotranspiration, are central to soil moisture trends. Where precipitation has already declined, an increase in its temporal concentration can amplify soil drying. Where precipitation is increasing, the same shift can dampen the resulting wetting, or even reverse it into net drying, thereby explaining the paradoxical drying under wetter conditions.

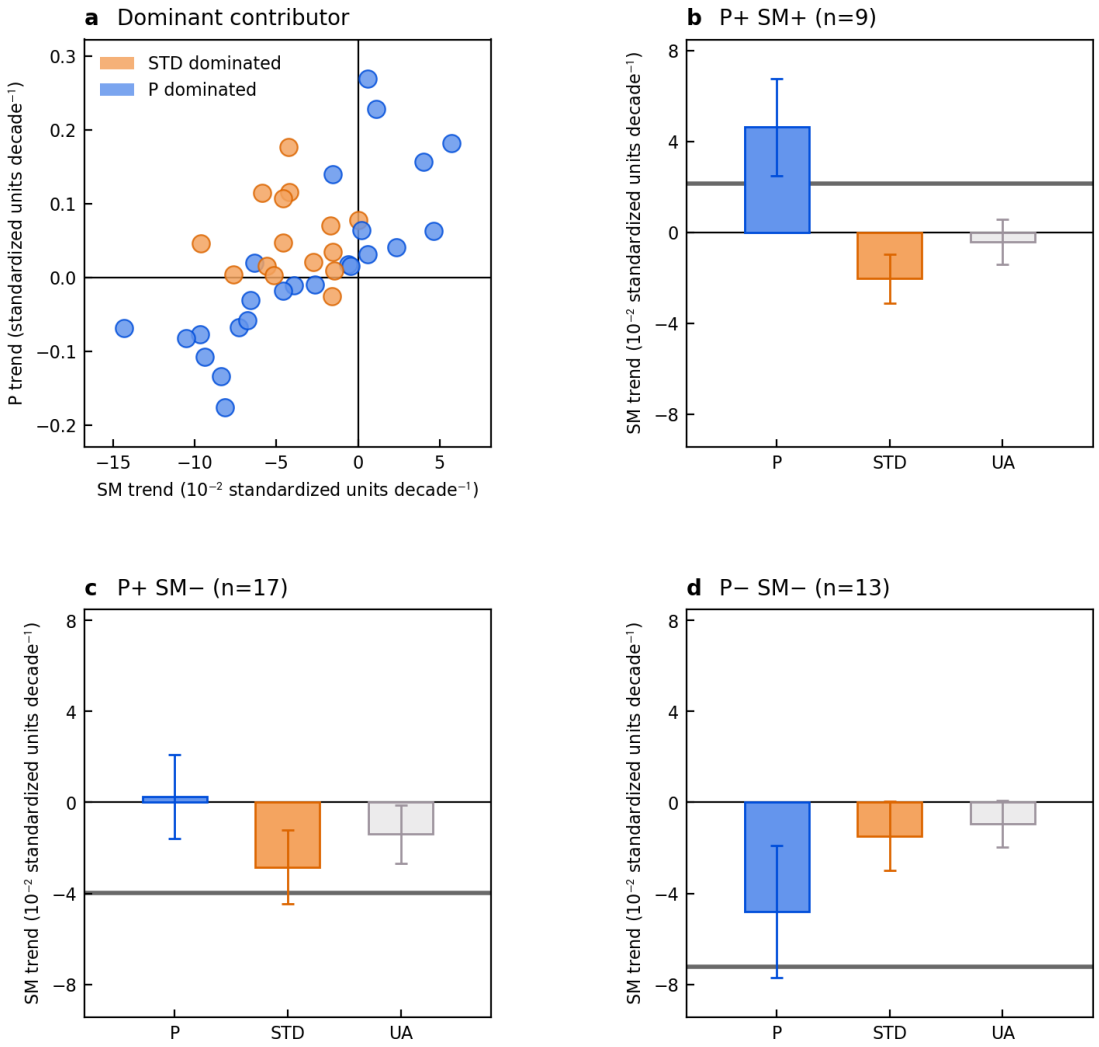


Fig. 2 | Precipitation unevenness drives soil moisture deficits across different regimes. **a**, Relationship between annual trends in soil moisture (SM) and precipitation amount (P) for all land regions with cross-product agreements. Point colors indicate the dominant driver of the SM trend (defined as STD-dominated when |STD contribution| > |P contribution|; otherwise, P-dominated). Zero lines divide the four hydrological regimes defined by the signs of P and SM trends. **b**, **c**, **d,** SHAP (Shapley Additive Explanations; see Methods) decomposition of the SM trend for the consistent wetting regime (P+SM+), the paradoxical regime (P+SM−) and the consistent drying regime (P−SM−). Bars show the mean contributions of total precipitation (blue), precipitation unevenness (orange), and the unattributed component (UA, grey). Error bars indicate the standard deviation, and grey lines mark the mean observed SM trend for the regime. The x-axis lists contributing factors.

Redistribution of hydrological states

By partitioning precipitation into different intensity classes, we quantify how much each class contributes to the increased unevenness. We find that the increase of

unevenness comes predominantly from heavy-rainfall events in the tail of the distribution (here defined as the 65th–100th percentile) rather than from ordinary rain days within the paradoxical regime (Fig. 3a, see Methods). The most extreme 1% (99th–100th) accounts for 63.89% of the total, and the heavy class as a whole contributes 89.92%, indicating that the increase in the heavy precipitation is the main driver of the increased precipitation unevenness in the paradoxical regime.

To understand how this heavy-rainfall-driven unevenness affects soil moisture, Figure 3b further shows the shift in precipitation distribution within the paradoxical regime. Precipitation distribution is becoming more polarized, as reflected in changes in both annual frequencies and total amounts across intensity classes. Dry days are increasing by 4.12 days per decade, while the heavy class is rising by 1.35 days per decade. In contrast, low- to moderate-intensity days (0–65th) decline markedly, with the weakest class (0–35th) showing the largest decrease at 4.49 days per decade. Although the increase in heavy-rainfall frequency is relatively small, the annual precipitation amount contributed by this class increases by a substantial 29.86 mm yr^{-1} $decade^{-1}$, exceeding the net increase in total annual precipitation (28.42 mm yr^{-1} $decade^{-1}$).

Increased high-intensity rainfall may not effectively moisten the soil. Instead, it can be lost as surface runoff or rapid drainage owing to the soil's limited water storage capacity. Therefore, we examine whether heavy rainfall can exceed the threshold for soil moisture saturation (here defined as soil water content at or above the 99th percentile of each site's climatology), finding that on 73.5% of soil-saturation days,

precipitation intensity exceeds the 65th percentile of its climatology (Fig. 3c, see Methods). This indicates that rainfall events above this intensity often deliver more water than is needed to saturate the soil. In other words, intensified heavy precipitation (65th–100th percentile) tends to be wasted as ineffective precipitation once the soil becomes saturated.

Most paradoxical regions show soil-saturating precipitation (P_{sat}, the heavy class defined above) increasing faster than total precipitation (i.e. the ratio of the P_{sat} trend to the precipitation trend exceeds 1.0), indicating that a larger share of the increased rainfall is delivered in runoff-prone heavy events (Fig. 3d). We further examine the relationship between this ratio and annual mean soil moisture, finding that a higher ratio corresponds to stronger drying: mean soil moisture declines by about 1.73×10^{-4} m^3 m^{-3} per decade for every 0.1 increase in the ratio. In certain regions, owing to differences in climatic background, the 65th-percentile threshold does not necessarily correspond to soil moisture saturation, which may explain why the ratio falls below 1.0 there. Nevertheless, the results remain consistent when different P_{sat} thresholds are used.

On the other hand, a disproportionate increase in heavy rainfall (ratio > 1) also means fewer low- to moderate-intensity precipitation days and longer rain-free spells, which reduce the replenishment of soil water and thus drive overall soil drying. For the dry extreme, a 0.1 rise in the ratio corresponds to roughly 0.47 more days per decade during which soil moisture remains below its 20th percentile (Supplementary Fig. 8).

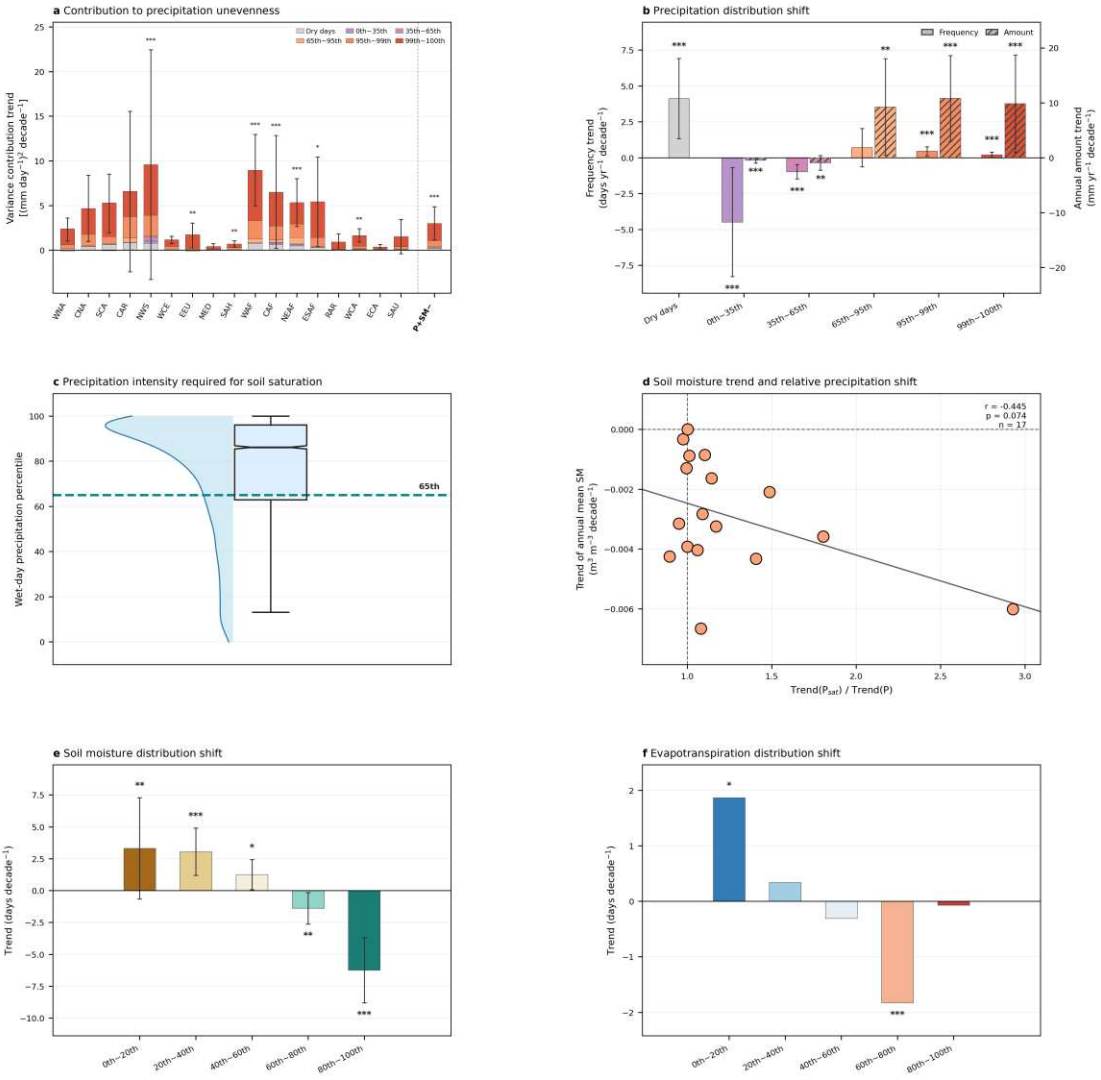


Fig. 3 | Hydrologic redistribution in the paradoxical P+SM− regime.

a, Regional decomposition of trends in daily precipitation variance (squared precipitation unevenness, see Methods) in the 17 P+SM− regions. Colors indicate contributions of dry days and five wet-day intensity categories. The rightmost bar shows the regime mean. **b,** Solid bars show decadal trends in annual number of days in each category (left axis), and hatched bars show decadal trends in annual precipitation amount contributed by each wet-day category (right axis). **c,** Distribution of wet-day precipitation percentiles on soil-saturation days at global FLUXNET sites, shown as a half-violin and box plot. **d,** Relationship between Trend(P_{sat})/Trend(P) and the annual mean soil moisture trend across the P+SM− regions. P_{sat} denotes soil-saturating precipitation (65th–100th wet-day percentiles), and P denotes total precipitation. The solid line shows the linear fit. **e,** Decadal trends in annual number of days in each soil moisture category in the P+SM− regions. **f,** As in **e,** but for evapotranspiration categories. Analyses cover 2000–2023. Bars in **a, b,** and **e** show means across datasets; error bars indicate ±1 standard deviation across datasets. Asterisks denote ordinary least-squares trend significance: *p < 0.05, **p < 0.01, ***p < 0.001.

Overall, the unevenness of precipitation, manifested as a polarization of the

distribution, has reshaped the soil-moisture distribution in the paradoxical regime. As rainless days grow more frequent and rainfall shifts further toward heavy events, the soil spends markedly more time in extremely dry states, while the time in the wet states is correspondingly shortened (Fig. 3e). As a result, the annual mean soil moisture declines even though total precipitation increases. This decline propagates to evapotranspiration, with low-evapotranspiration states becoming more common and high-evapotranspiration states rarer (Fig. 3f). Correspondingly, the annual total evapotranspiration decreases (-3.00 mm decade^{-1}) over the paradoxical regime, indicating that it is not the actual driver of the soil moisture decline.

These findings reveal the key role of enhanced precipitation unevenness in driving soil drying. Nevertheless, in real-world observations, other processes, such as increased evaporative demand driven by global warming, also contribute to soil drying. To test whether these observed changes can be produced by precipitation unevenness alone, we design an idealized single-layer bucket-model experiment with the *Even* and *Uneven* rainfall scenarios (Fig. 4, see Methods). Both scenarios use the same 900 mm total and differ only in how rainfall is distributed over time, with precipitation unevenness of 10.0 mm and 16.0 mm in the *Even* and *Uneven* scenarios respectively. Rainfall is apportioned into many light spells in the *Even* scenario (Fig. 4a), while in the *Uneven* scenario, it falls in a few intense bursts (Fig. 4b). Relative to the *Even* scenario, runoff in the *Uneven* scenario increases roughly fourfold (from 121.38 to 489.33 mm; Fig. 4c), while the effective precipitation retained in the soil decreases by about 47% (from 778.62 to 410.67 mm). As a result, soil moisture in the *Uneven* scenario decreases by

about 41% relative to the *Even* scenario (from 29.7% to 17.6%, Fig. 4a, b). Meanwhile, consistent with the observations, the soil moisture distribution shifts toward longer dry periods and shorter wet periods (Fig. 4d), with more low-evapotranspiration days (Fig. 4e). These results are consistent with 300 parameter perturbations (Fig. 4f–h), indicating that concentration of the temporal structure of precipitation alone is sufficient to reduce effective precipitation through runoff losses and to reshape the soil moisture and evapotranspiration distributions.

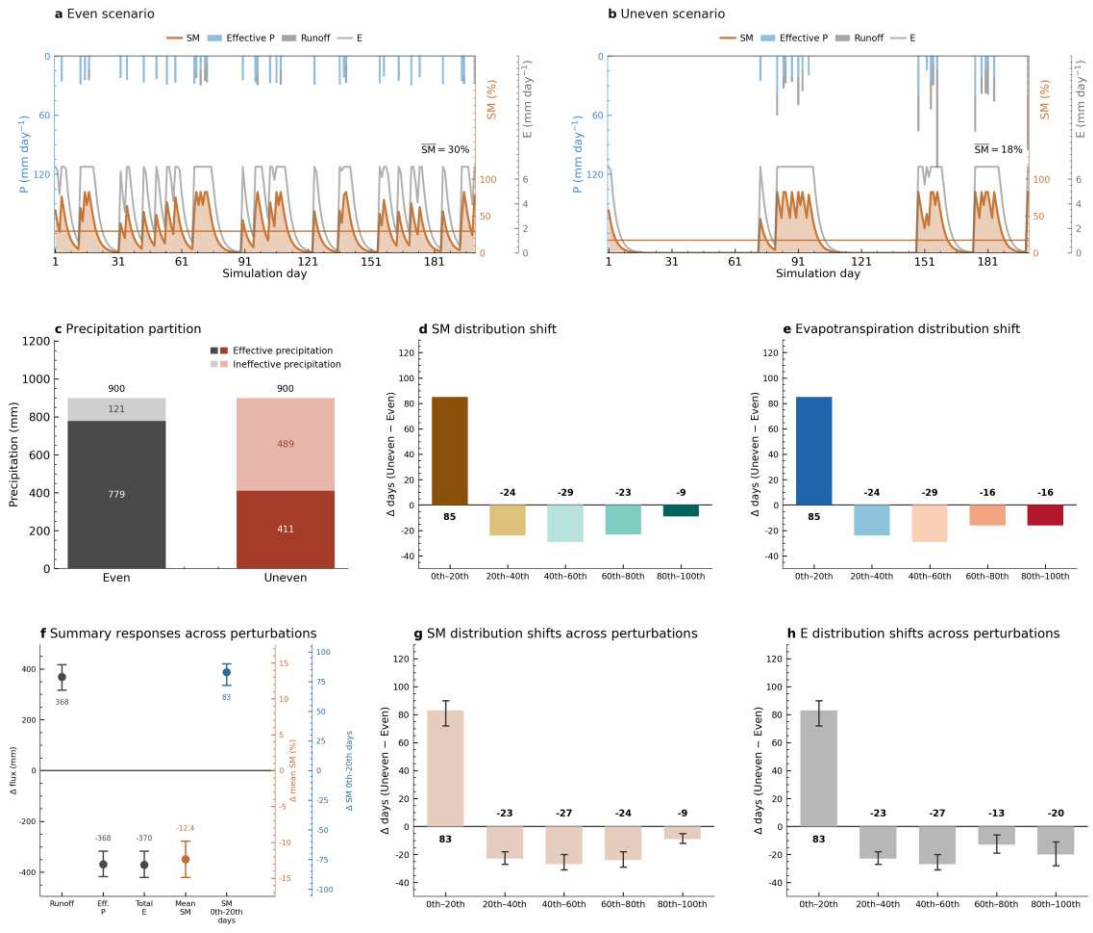


Fig. 4 | Effects of precipitation unevenness in an idealized bucket model.

Precipitation *(P)* partitioning, soil moisture (*SM*), and evapotranspiration (*E*) are compared between the *Even* and *Uneven* scenarios, which differ only in precipitation unevenness (see Methods). **a, b,** Daily time series of *P*, *SM*, and *E* in the Even (**a**) and Uneven (**b**) scenarios. Precipitation is separated into effective (blue bars) and ineffective (runoff, grey bars) components. The orange line and shading show *SM*, and the grey line shows *E*. **c,** Total effective

and total ineffective precipitation in each scenario. **d, e,** Bars show *Uneven* − *Even* differences in the number of days within SM (**d**) and E (**e**) quintile bins. Bins are defined using the corresponding *Even*-scenario distribution; positive values indicate more days in the *Uneven* scenario. **f–h,** Robustness of *Uneven* − *Even* to parameter perturbations in a 300-member ensemble. Points and bars show medians and whiskers span the 5th to 95th percentiles. **f,** Differences in total runoff, effective precipitation, and evapotranspiration (mm), together with mean SM (percentage points) and days in the lowest SM quintile. **g, h,** Differences in the number of days within SM (**g**) and E (**h**) quintile bins.

Discussion

This study reveals the key role of enhanced precipitation unevenness in shaping the paradox of rising precipitation yet declining soil moisture. Across the paradoxical regions that cover about 42.4% of the global land area, the soil moisture decline driven by enhanced precipitation unevenness is about eleven times as large as the wetting effect of increased total precipitation, producing a pronounced overall drying of soil moisture. This enhanced unevenness stems mainly from the growing share of heavy precipitation. By lowering the rainfall-to-soil-moisture conversion efficiency and increasing the number of dry days, it holds soil moisture in dry states for longer and reshapes the distribution of soil moisture. Our idealized model experiment further confirms that precipitation unevenness alone can drive these changes in the soil moisture distribution.

Notably, by redistributing rainfall from moderate, infiltration-effective events toward runoff-prone heavy episodes[32], intensified unevenness not only suppresses recovery from droughts but simultaneously heightens the risk of floods. This echoes the frequent compound extremes[33,34] and "weather whiplash" events[35,36] observed in recent years, highlighting the dual burdens and high vulnerability faced by ecosystems and human societies. For example, in 2022, Southwest China experienced severe extreme

rainfall following prolonged precipitation deficits[34]. The combination of soil droughts, heatwaves, and floods caused local ecosystem disruption and temporary energy shortages, with aggregate consequences substantially exceeding those of individual extreme events. More concerningly, this hydrological paradox may extend beyond the past two decades, becoming the new norm for terrestrial hydrology under future climate scenarios. As warming continues, total precipitation will keep increasing, while extreme precipitation is projected to increase even more strongly[37–39], likely exacerbating precipitation unevenness and the associated soil drying. The mismatch between precipitation input and soil water storage may therefore continue to widen, exposing traditionally secure regions to unprecedented water stress.

In this wetter yet drier world, the increase in annual precipitation totals may no longer be a favorable signal for areas with a more uneven precipitation distribution. Therefore, intensifying precipitation unevenness should be considered a key indicator for projecting climate extremes, complementing traditional reliance on total rainfall. As extreme events sharply rise, conventional climate indices based on precipitation amounts—such as the Köppen climate classification[40] and Aridity Index[41]—may fail to accurately represent local climate realities. Many humid regions (e.g., the Mediterranean and central North America) are experiencing unprecedented droughts, heatwaves, floods, and even ecosystem collapse[42–45], breaking the traditional boundaries between dry and humid climates. Consequently, we advocate for the integration of unevenness metrics into climate monitoring frameworks. Systematically tracking hydrological variability with these tools can enable more timely adaptation

289 strategies and bolster resilience against climate change.

Methods

Data

The primary datasets used in this study include precipitation data from CPC (0.5° × 0.5°)[46], CHIRPS (0.05° × 0.05°)[47,48], and MSWEP (0.1° × 0.1°)[49] (see Supplementary Table 1), and surface soil moisture data from ERA5 (0.25° × 0.25°)[50], ERA5-Land (0.1° × 0.1°)[51], ESA CCI (0.25° × 0.25°)[52], GLDAS-Noah (1° × 1°)[53], and GLEAM4 (0.1° × 0.1°)[54] (see Supplementary Table 2). Evapotranspiration data are obtained from ERA5 (0.25° × 0.25°). These datasets have been widely used and evaluated[55–58]. The analysis focuses on the period 2000–2023 and on the land areas between 60°S and 85°N, excluding Greenland, Iceland and major inland water bodies.

We construct ensemble means of precipitation, soil moisture, and precipitation unevenness using the products described above. For each product, annual values are first calculated at the grid-cell level and then averaged within each AR6 land region using area weights. To place the products on a common scale, the regional annual values for each product are standardized and then averaged with equal weights across all available products to construct the ensemble. Because CHIRPS v3 is limited to 60°S–60°N, the precipitation and precipitation unevenness ensembles for the Russian Arctic (RAR) include only CPC and MSWEP. For calculations using individual datasets, soil moisture units are unified as $m^3\ m^{-3}$ (volumetric water content).

Temporal unevenness of precipitation and intensity-based decomposition

At grid cell g in year y, annual precipitation unevenness is quantified using the

standard deviation of daily precipitation. This index, denoted by *STD*, is defined as:

$$STD_{g,y} = \sqrt{VAR_{g,y}} = \sqrt{\frac{1}{n}\sum_{d=1}^{n}(p_d - \bar{p})^2} \quad (1)$$

where *VAR* is precipitation variance, n is the number of days in year y, p_d is the precipitation amount on day d, and $\bar{p}$ is the mean daily precipitation amount in year y. Because all days of the year are considered, dry days (p_d=0) also contribute to precipitation unevenness.

For each AR6 region r, the regional unevenness $STD_{r,y}$ is defined as the square root of the area-weighted mean of *VAR* over valid land grid cells within the region. Due to the decomposability of *VAR*, we partition the daily precipitation intensity into different categories $C_1 \ldots C_6$: dry days and five wet-day ($p_d > 0$) intensity classes, with the wet days further stratified by their climatological percentile over 2000–2023 into 0th–35th, 35th–65th, 65th–95th, 95th–99th, and 99th–100th bins. This gives the decomposition:

$$STD^2 = VAR = \sum_{i=1}^{6} VAR_{C_i}, \qquad VAR_{C_i} = \frac{1}{n}\sum_{d \in C_i}(p_d - \bar{p})^2 \quad (2)$$

Further, for a time series x, we denote its ordinary least squares trend (OLS) as $T(x)$. Since OLS trend estimation is linear, this gives:

$$T(STD^2) = T(VAR) = \sum_{i=1}^{6} T\left(VAR_{C_i}\right) \quad (3)$$

Thus the contributions of different intensity categories to the overall trend in unevenness can be quantified.

Random forest

To examine how precipitation characteristics influence *SM*, we construct a year × region panel covering all 43 land regions globally over 24 years. *SM* is the response

variable, and the two predictors are annual total precipitation *P* and annual precipitation unevenness *STD*. All variables use the standardized multi-product ensemble means described above.

For each region we remove the climatological mean of every variable. A Random Forest model[59] is then trained to predict the regional soil moisture anomaly *SM'* from the regional anomalies of precipitation amount and unevenness, *P'* and *STD'*. Adding the predicted anomaly $\widehat{SM'}$ back to the regional mean yields the predicted soil moisture $\widehat{SM}$. This design absorbs persistent regional differences such as climatological soil moisture, vegetation, soil properties, and other slowly varying geographic controls. Observed and predicted SM time series agree closely (Supplementary Figs. 5–7), showing that the model robustly reproduces interannual soil moisture variability.

To interpret the model, we apply the tree-based Shapley additive explanations method (TreeSHAP[60]) with path-dependent feature perturbation, which splits the prediction for each sample into additive contributions. Let $\widehat{SM'_i}$ denote the prediction for sample *i*. The decomposition gives:

$$\widehat{SM'_i} = \phi_0 + \phi_{i,P} + \phi_{i,STD} \quad (4)$$

where ϕ_0 is the model baseline, equal to $\overline{SM'}$, and is constant across all samples. Because anomalies are used in this model, ϕ_0 equals zero. The SHAP values $\phi_{i,P}$ and $\phi_{i,STD}$ quantify the signed additive contributions of *P* and *STD* for sample *i*. All terms have the same standardized units as soil moisture anomalies. The decomposition is additive, supporting summary analyses across time, regions, or both, and can isolate the

independent effects of interannual variability in *P* and *STD* on *SM*.

We decompose the predicted soil moisture $\widehat{SM}$ trends for each region into:

$$T\left(\widehat{SM}\right) = T\left(\widehat{SM'}\right) = T(\phi_P) + T(\phi_{STD}) \quad (5)$$

where $T(\phi_P)$ and $T(\phi_{STD})$ are the contributions of total precipitation and precipitation unevenness, respectively.

We define the unattributed (*UA*) trend as the portion of the observed soil moisture trend not explained by total precipitation or unevenness:

$$UA = T(SM) - T(\phi_P) - T(\phi_{STD}) \quad (6)$$

The *UA* component includes residual model–observation mismatches. This decomposition allows clear quantification of the respective contributions of precipitation amount and unevenness to observed soil moisture trends.

Soil-saturating precipitation

To evaluate the rainfall intensity linked to soil moisture saturation, we use daily precipitation and shallow soil water content data (SWC_F_MDS_1, ~5 cm depth) from FLUXNET[61]. We set the soil saturation threshold as the 99th percentile of the site's historical values (2000–2023). A soil saturation day is defined as a day when the soil moisture goes from being below the 99th percentile on the previous day to being at or above the 99th percentile on the current day. In total, 5365 soil-saturation days across 551 sites are identified (Supplementary Fig. 9). On 3945 soil-saturation days (73.5% of all), precipitation intensity exceeded the 65th percentile. Hence we define precipitation in the 65th–100th percentile range as soil-saturating precipitation.

Idealized bucket model

We use an idealized single-layer bucket model to isolate the effect of precipitation unevenness on soil moisture under fixed total precipitation and evaporative demand. Single-layer bucket models are widely used to simulate the land surface water balance [62,63] and generally show good agreement with observations[64,65].

The model is updated at a daily time step. P_t denotes precipitation on day t, S_t denotes end-of-day water storage, S_0 denotes initial storage, and S_{max} denotes the maximum storage capacity. In this model, S_0 and S_{max} are set to 30 and 40 mm, respectively. Soil moisture SM_t is calculated as S_t/S_{max} and expressed as a percentage. Although the model does not include vegetation, evaporative water loss is referred to as actual evapotranspiration E_t for consistency with the terminology used throughout the study. On each day, precipitation first replenishes soil-water storage. Precipitation is retained as effective precipitation until storage reaches S_{max}, whereas any excess becomes runoff, here termed ineffective precipitation. Water then leaves the bucket through actual evapotranspiration E_t. E_t equals the prescribed evaporative demand when soil-water storage exceeds the critical threshold S^*, set to 60% of S_{max}, but is limited by available soil water when storage is below this threshold. After evapotranspiration, the remaining water is recorded as the end-of-day storage S_t.

We compare two prescribed scenarios, *Even* and *Uneven*, over 200-day runs. Both scenarios have a total precipitation of 900.0 mm and the same constant evaporative demand of 7.0 mm day^{-1}, but differ only in precipitation unevenness. The standard

396 deviation of daily precipitation is 10.0 mm in the *Even* scenario and 16.0 mm in the
397 *Uneven* scenario.

398 To assess robustness, we run a 300-member perturbation ensemble while keeping
399 total precipitation fixed at 900.0 mm. We perturb evaporative demand, maximum
400 storage capacity S_{max}, initial storage S_0, critical threshold S^*, and the timing and
401 amounts of individual precipitation events. The ensemble results are shown in Fig. 4f–
402 h.

References

1. Deng, Y. et al. Variation trend of global soil moisture and its cause analysis. *Ecol. Indic.* **110**, 105939 (2020).
2. Lal, P., Shekhar, A., Gharun, M. & Das, N. N. Spatiotemporal evolution of global long-term patterns of soil moisture. *Sci. Total Environ.* **867**, 161470 (2023).
3. Seo, K.-W. et al. Abrupt sea level rise and Earth's gradual pole shift reveal permanent hydrological regime changes in the 21st century. *Science* **387**, 1408–1413 (2025).
4. Seo, Y.-W. & Ha, K.-J. Changes in land-atmosphere coupling increase compound drought and heatwaves over northern East Asia. *npj Clim. Atmos. Sci.* **5**, 100 (2022).
5. Maraun, D., Schiemann, R., Ossó, A. & Jury, M. Changes in event soil moisture-temperature coupling can intensify very extreme heat beyond expectations. *Nat. Commun.* **16**, 734 (2025).
6. Zhang, K., Zuo, Z., Mei, W., Zhang, R. & Dai, A. A westward shift of heatwave hotspots caused by warming-enhanced land–air coupling. *Nat. Clim. Change* **15**, 546–553 (2025).
7. Zhang, P. et al. Abrupt shift to hotter and drier climate over inner East Asia beyond the tipping point. *Science* **370**, 1095–1099 (2020).
8. Padrón, R. S. et al. Observed changes in dry-season water availability attributed to human-induced climate change. *Nat. Geosci.* **13**, 477–481 (2020).
9. Heino, M. et al. Increased probability of hot and dry weather extremes during the growing season threatens global crop yields. *Sci. Rep.* **13**, 3583 (2023).
10. Allen, C. D. et al. A global overview of drought and heat-induced tree mortality reveals emerging climate change risks for forests. *For. Ecol. Manage.* 259, 660–684 (2010).
11. Gu, G. & Adler, R. F. Observed variability and trends in global precipitation during 1979–2020. *Clim. Dyn.* **61**, 131–150 (2023).

12. Allen, M. R. & Ingram, W. J. Constraints on future changes in climate and the hydrologic cycle. *Nature* 419, 224–232 (2002).
13. Harp, R. D. & Horton, D. E. Observed changes in interannual precipitation variability in the United States. *Geophys. Res. Lett.* **50**, e2023GL104533 (2023).
14. McDonough, K. R., Hutchinson, S. L. & Hutchinson, S. Declining soil moisture threatens water availability in the U.S. Great Plains. *Trans. ASABE* **63**, 1147–1156 (2020).
15. Zhang, M., Chen, Y., Shen, Y. & Li, Y. Changes of precipitation extremes in arid Central Asia. *Quat. Int.* **436**, 16–27 (2017).
16. Amantai, N., Meng, Y., Wang, J., Ge, X. & Tang, Z. Climate overtakes vegetation greening in regulating spatiotemporal patterns of soil moisture in arid Central Asia in recent 35 years. *GISci. Remote Sens.* **61**, 2286744 (2024).
17. Rajah, K. et al. Changes to the temporal distribution of daily precipitation. *Geophys. Res. Lett.* **41**, 8887–8894 (2014).
18. Konapala, G., Mishra, A. & Leung, L. R. Changes in temporal variability of precipitation over land due to anthropogenic forcings. *Environ. Res. Lett.* **12**, 024009 (2017).
19. Chen, Y. Increasingly uneven intra-seasonal distribution of daily and hourly precipitation over Eastern China. *Environ. Res. Lett.* **15**, 104068 (2020).
20. Zhang, W. et al. Increasing precipitation variability on daily-to-multiyear time scales in a warmer world. *Sci. Adv.* **7**, eabf8021 (2021).
21. Duan, W. et al. Changes in temporal inequality of precipitation extremes over China due to anthropogenic forcings. *npj Clim. Atmos. Sci.* **5**, 33 (2022).
22. Goffin, B. D., Kansara, P. & Lakshmi, V. Intensification in the Wettest Days to 50 Percent of Annual Precipitation (WD50) Across Europe. *Geophys. Res. Lett.* **51**, e2023GL107403 (2024).
23. Zhang, W., Zhou, T. & Wu, P. Anthropogenic amplification of precipitation variability over the past century. *Science* **385**, 427–432 (2024).
24. Lesk, C. S. & Mankin, J. S. More concentrated precipitation decreases terrestrial water storage. *Nature* **653**, 425–432 (2026).

461 25. Qing, Y. et al. Accelerated soil drying linked to increasing evaporative demand
462 in wet regions. *npj Clim. Atmos. Sci.* **6**, 205 (2023).
463 26. Qing, Y., Wang, S., Ancell, B. C. & Yang, Z.-L. Accelerating flash droughts
464 induced by the joint influence of soil moisture depletion and atmospheric aridity.
465 *Nat. Commun.* **13**, 1139 (2022).
466 27. Kim, S., Anabalón, A. & Sharma, A. An Assessment of Concurrency in
467 Evapotranspiration Trends across Multiple Global Datasets. *J. Hydrometeorol.*
468 **22**, 231–244 (2021).
469 28. Cai, Y. et al. Reconciling Global Terrestrial Evapotranspiration Estimates From
470 Multi-Product Intercomparison and Evaluation. *Water Resour. Res.* **60**,
471 e2024WR037608 (2024).
472 29. Saxton, K. E. & Rawls, W. J. Soil Water Characteristic Estimates by Texture and
473 Organic Matter for Hydrologic Solutions. *Soil Sci. Soc. Am. J.* **70**, 1569–1578
474 (2006).
475 30. Fu, Z. et al. Global critical soil moisture thresholds of plant water stress. *Nat.*
476 *Commun.* **15**, 4826 (2024).
477 31. Iturbide, M. et al. An update of IPCC climate reference regions for subcontinental
478 analysis of climate model data: definition and aggregated datasets. *Earth Syst. Sci.*
479 *Data* 12, 2959–2970 (2020).
480 32. Knapp, A. K. et al. Consequences of More Extreme Precipitation Regimes for
481 Terrestrial Ecosystems. *BioScience* 58, 811–821 (2008).
482 33. Deng, S. et al. Global Distribution and Projected Variations of Compound
483 Drought-Extreme Precipitation Events. *Earth's Future* **12**, e2024EF004809
484 (2024).
485 34. Hao, Z., Chen, Y., Feng, S., Liao, Z., An, N. & Li, P. The 2022 Sichuan-
486 Chongqing spatio-temporally compound extremes: a bitter taste of novel hazards.
487 *Sci. Bull.* 68, 1337–1339 (2023).
488 35. Tan, X. et al. Increasing global precipitation whiplash due to anthropogenic
489 greenhouse gas emissions. *Nat. Commun.* 14, 2796 (2023).

490 36. Swain, D. L. et al. Hydroclimate volatility on a warming Earth. *Nat. Rev. Earth*
491 *Environ.* 6, 35–50 (2025).
492 37. Gründemann, G. J., van de Giesen, N., Brunner, L. & van der Ent, R. Rarest
493 rainfall events will see the greatest relative increase in magnitude under future
494 climate change. *Commun. Earth Environ.* **3**, 235 (2022).
495 38. Thackeray, C. W., Hall, A., Norris, J. & Chen, D. Constraining the increased
496 frequency of global precipitation extremes under warming. *Nat. Clim. Change* **12**,
497 441–448 (2022).
498 39. Zhou, W., Leung, L. R., Siler, N. & Lu, J. Future precipitation increase
499 constrained by climatological pattern of cloud effect. *Nat. Commun.* **14**, 6363
500 (2023).
501 40. Peel, M. C., Finlayson, B. L. & McMahon, T. A. Updated world map of the
502 Köppen-Geiger climate classification. *Hydrol. Earth Syst. Sci.* **11**, 1633–1644
503 (2007).
504 41. Zomer, R. J., Xu, J. & Trabucco, A. Version 3 of the Global Aridity Index and
505 Potential Evapotranspiration Database. *Sci. Data* 9, 409 (2022).
506 42. Jin, C. et al. The 2012 flash drought threatened US Midwest agroecosystems. *Chin.*
507 *Geogr. Sci.* **29**, 768–783 (2019).
508 43. Bevacqua, E. et al. Direct and lagged climate change effects intensified the 2022
509 European drought. *Nat. Geosci.* **17**, 1100–1107 (2024).
510 44. Lemus-Canovas, M., Insua-Costa, D., Trigo, R. M. & Miralles, D. G. Record-
511 shattering 2023 spring heatwave in western Mediterranean amplified by long-
512 term drought. *npj Clim. Atmos. Sci.* **7**, 25 (2024).
513 45. Alderotti, F. et al. Linking patterns of forest dieback to triggering climatic and
514 weather events: an overview on Mediterranean forests. *iForest* **17**, 309–316
515 (2024).
516 46. Chen, M. et al. Assessing objective techniques for gauge-based analyses of global
517 daily precipitation. *J. Geophys. Res. Atmos.* **113**, D04110 (2008).
518 47. Funk, C. et al. The climate hazards infrared precipitation with stations—a new
519 environmental record for monitoring extremes. *Sci. Data* **2**, 150066 (2015).

48. Funk, C. et al. The Climate Hazards Center Infrared Precipitation with Stations, Version 3. *Sci. Data* 13, 718 (2026).
49. Beck, H. E. et al. MSWEP V2 Global 3-Hourly 0.1° Precipitation: Methodology and Quantitative Assessment. *Bull. Am. Meteorol. Soc.* **100**, 473–500 (2019).
50. Hersbach, H. et al. The ERA5 global reanalysis. *Q. J. R. Meteorol. Soc.* **146**, 1999–2049 (2020).
51. Muñoz-Sabater, J. et al. ERA5-Land: a state-of-the-art global reanalysis dataset for land applications. *Earth Syst. Sci. Data* **13**, 4349–4383 (2021).
52. Dorigo, W. et al. ESA CCI Soil Moisture for improved Earth system understanding: State-of-the art and future directions. *Remote Sens. Environ.* **203**, 185–215 (2017).
53. Rodell, M. et al. The Global Land Data Assimilation System. *Bull. Am. Meteorol. Soc.* 85, 381–394 (2004).
54. Miralles, D. G. et al. GLEAM4: global land evaporation and soil moisture dataset at 0.1° resolution from 1980 to near present. *Sci. Data* **12**, 416 (2025).
55. Beck, H. E. et al. Global-scale evaluation of 22 precipitation datasets using gauge observations and hydrological modeling. *Hydrol. Earth Syst. Sci.* 21, 6201–6217 (2017).
56. Beck, H. E. et al. Evaluation of 18 satellite- and model-based soil moisture products using in situ measurements from 826 sensors. *Hydrol. Earth Syst. Sci.* 25, 17–40 (2021).
57. Zhu, Z. et al. Global soil moisture dynamics since 1980: datasets biases, trends, and science-informed selection. *Sci. Bull.* **70**, 4253–4262 (2025).
58. Martens, B. et al. Evaluating the land-surface energy partitioning in ERA5. *Geosci. Model Dev.* 13, 4159–4181 (2020).
59. Breiman, L. Random Forests. *Mach. Learn.* **45**, 5–32 (2001).
60. Lundberg, S. M. et al. From local explanations to global understanding with explainable AI for trees. *Nat. Mach. Intell.* **2**, 56–67 (2020).
61. Pastorello, G. et al. The FLUXNET2015 dataset and the ONEFlux processing pipeline for eddy covariance data. *Sci. Data* **7**, 225 (2020).

62. Manabe, S. Climate and the Ocean Circulation: I. The Atmospheric Circulation and the Hydrology of the Earth's Surface. *Mon. Weather Rev.* **97**, 739–774 (1969).
63. Romano, N., Palladino, M. & Chirico, G. B. Parameterization of a bucket model for soil-vegetation-atmosphere modeling under seasonal climatic regimes. *Hydrol. Earth Syst. Sci.* **15**, 3877–3893 (2011).
64. Fan, Y. & van den Dool, H. Climate Prediction Center global monthly soil moisture data set at 0.5° resolution for 1948 to present. *J. Geophys. Res. Atmos.* **109**, D10102 (2004).
65. Robock, A., Vinnikov, K. Ya., Schlosser, C. A., Speranskaya, N. A. & Xue, Y. Use of Midlatitude Soil Moisture and Meteorological Observations to Validate Soil Moisture Simulations with Biosphere and Bucket Models. *J. Clim.* **8**, 15–35 (1995).

Acknowledgments

Funding

This work was jointly supported by the National Natural Science Foundation of China (Grant No. 42288101), the National Key Research and Development Program (Grant No. 2022YFF0801703), and Tsinghua University (100008001).

Author contributions

S.C., M.C. and Z.Z. designed the study. S.C. conducted the analysis. Z.Z., M.C., D.C., and R.Z. advised on the interpretation of the results. S.C., M.C., K.Z., and D.C. wrote the manuscript. K.Z. and S.C. developed the methods.

Competing interests

The authors declare no competing interests.

Data availability

All data used in this study are freely available online. The AR6 land reference regions dataset can be accessed through the regionmask Python package (https://regionmask.readthedocs.io/). The CHIRPS dataset can be downloaded from the Climate Hazards Center at the University of California, Santa Barbara (https://www.chc.ucsb.edu/data/chirps3). The CPC Unified Gauge-Based Analysis of Global Daily Precipitation dataset can be downloaded from NOAA Climate Prediction Center (https://ftp.cpc.ncep.noaa.gov/precip/CPC_UNI_PRCP/GAUGE_GLB/). The ERA5 dataset can be downloaded from the Copernicus Climate Data Store (https://cds.climate.copernicus.eu/datasets/reanalysis-era5-single-levels). The ERA5-Land dataset can be downloaded from the Copernicus Climate Data Store

(https://cds.climate.copernicus.eu/datasets/reanalysis-era5-land-monthly-means?tab=download). The ESA CCI Soil Moisture dataset can be downloaded from the ESA Climate Change Initiative Soil Moisture data portal (https://climate.esa.int/en/projects/soil-moisture/). The FLUXNET/FLUXMET daily dataset can be downloaded from the FLUXNET data portal (https://data.fluxnet.org/), subject to the FLUXNET access and redistribution terms. The GLDAS-Noah dataset can be downloaded from NASA Goddard Earth Sciences Data and Information Services Center (https://disc.gsfc.nasa.gov/datasets?keywords=GLDAS). The GLEAM4 dataset can be downloaded from the Global Land Evaporation Amsterdam Model website (https://www.gleam.eu/#downloads). The MSWEP v3.15 dataset can be downloaded from GloH2O (https://www.gloh2o.org/mswep/). The Natural Earth land dataset can be downloaded from Natural Earth (https://www.naturalearthdata.com/downloads/).

Code availability

All analyses and figures were generated using Python 3.11.9. Code is available upon request.

Supplementary Materials

Supplementary Figs. 1–9 and Supplementary Tables 1–3.

Supplementary Files

This is a list of supplementary files associated with this preprint. Click to download.

- Supplyment.docx